The Spitzer Space Telescope First-Look Survey: KPNO MOSAIC-1 R-band Images and Source Catalogs

Dario Fadda[1], Buell T. Jannuzi[2], Alyson Ford[2], Lisa J. Storrie-Lombardi[1]

ABSTRACT

We present R-band images covering more than 11 square degrees of sky that were obtained in preparation for the Spitzer Space Telescope First Look Survey (FLS). The FLS was designed to characterize the mid-infrared sky at depths 2 orders of magnitude deeper than previous surveys. The extragalactic component is the first cosmological survey done with *Spitzer*. Source catalogs extracted from the R-band images are also presented. The R-band images were obtained using the MOSAIC-1 camera on the Mayall 4m telescope of the Kitt Peak National Observatory. Two relatively large regions of the sky were observed to modest depth: the main FLS extra galactic field ($17^h18^m00^s$ $+59^o30'00''.0$ J2000; l= 88.3, b= +34.9) and ELAIS-N1 field ($16^h10^m01^s$ $+54^o30'36''.0$ J2000; l= 84.2, b= +44.9). While both of these fields were in early plans for the FLS, only a single deep pointing test observation was made at the ELAIS-N1 location. The larger Legacy program SWIRE (Lonsdale et al., 2003) will include this region among its surveyed areas. The data products of our KPNO imaging (images and object catalogs) are made available to the community through the World Wide Web (via the Spitzer Science Center and NOAO Science Archives). The overall quality of the images is high. The measured positions of sources detected in the images have RMS uncertainties in their absolute positions of order 0.35 arc-seconds with possible systematic offsets of order 0.1 arc-seconds, depending on the reference frame of comparison. The relative astrometric accuracy is much better than 0.1 of an arc-second. Typical delivered image quality in the images is 1.1 arc-seconds full width at half maximum. Images are relatively deep since they reach a median 5σ depth limiting magnitude of R=25.5 (Vega), as measured within a $1.35 \times$ FWHM aperture for which the S/N ratio is maximal. Catalogs have been extracted using SExtractor using thresholds in area and flux for which the number of false detections is below 1% at R=25. Only sources with S/N greater than 3 have been retained in the final catalogs. Comparing the galaxy number counts from our images with those of deeper R-band surveys, we estimate that our observations are 50% complete at R=24.5. These limits in depth are sufficient to identify a substantial fraction of the infrared sources which will be detected by *Spitzer*.

Subject headings: astronomical data bases:catalogs — galaxies: photometry

1. Introduction

One of the main advantages of the Spitzer Space Telescope (formerly known as the Space Infrared Infrared Telescope Facility; SIRTF, Gallagher et al. 2003) is the possibility to make extragalactic surveys of large regions of the sky in a relatively short time covering wavelengths from the near-IR to the far-IR with the instruments IRAC (Fazio et al. 1998) and MIPS (Rieke et al. 1996). Compared to *Spitzer*'s predecessors (e.g. IRAS, Soifer et al. 1983, and ISO, Kessler et al. 1996), there are improvements in the detectors (number of pixels and better responsivity), the collecting area of the primary mirror (85cm diameter), and Sun-Earth-Moon avoidance constraints due *Spitzer*'s helio-

[1]Spitzer Science Center, California Institute of Technology, MS 220-6, Pasadena, CA 91125

[2]National Optical Astronomy Observatory, Tucson, AZ 85719

centric orbit. *Spitzer* can also make observations simultaneously in multiple bands (with IRAC–3.6 and 4.5 or 5.8 and 8 μm; with MIPS–24, 70 and 160 μm).

Many extragalactic surveys are already scheduled with *Spitzer* as Legacy programs (SWIRE, Lonsdale et al. 2003; GOODS, Dickinson & Giavalisco 2001) or as observations by the Instrument Teams (Wide, Deep and Ultra-Deep *Spitzer* surveys which will cover regions like the Boötes field of the NOAO Deep Wide-Field Survey, the Groth strip, Lockman Hole, XMM-Deep and so on, see e.g. Dole et al. 2001). The First Look Survey utilizes 112 hours of Director's Discretionary time on *Spitzer* and includes extragalactic, galactic, and ecliptic components[1]. These data will be available to all observers when the Spitzer Science Archive opens in May, 2004. The purpose of the FLS is to characterize the mid-infrared sky at previously unexplored depths and make these data rapidly available to the astronomical community. The extragalactic component is comprised of a 4 square degree survey with IRAC and MIPS near the north ecliptic pole centered at J1718+5930. These observations were executed on 2003 December 1-11.

To fully exploit the *Spitzer* FLS data we have obtained ancillary surveys at optical (this paper) and radio wavelengths (Condon et al. 2003). Given the modest spatial resolution of the *Spitzer* imagers (the point spread function is large, especially in the mid and far-IR, e.g. 5.7 arcseconds full width at half maximum, FWHM, for the 24 μm channel), the first problem to solve for the infrared sources detected by *Spitzer* will be to associate these sources with an optical counterpart, when possible. This will then allow the higher spatial resolution of the available optical images to assist with the source classification (e.g. as stars, galaxies or QSO) and enable targeting of subsets of the sources for spectroscopy with optical or near-IR spectrographs. Since many of the infrared sources that will be detected by *Spitzer* will be dust-obscured galaxies with faint optical counterparts, the complementary optical imaging must be relatively deep.

Although a deep multi-wavelength optical survey would be more useful, allowing one to compute photometric redshifts (e.g. the NOAO Deep Wide-Field Survey, Jannuzi and Dey 1999, Brown et al. 2003), the task of deeply covering a large region of sky in a homogeneous manner is quite time-consuming. Therefore, for the initial optical ancillary survey we chose to observe the entire field in the R-band. NOAO provided 4 nights of Director's Discretionary time on the KPNO 4m in May, 2000, for this survey. We have limited multi-wavelength optical observations to the central portion of the FLS field. The Sloan Digital Sky Survey included the FLS field in their early release observations (Stoughton et al. 2002) and mosaics and catalogs for the region are also now available (Hogg et al. 2004).

In this paper, we present the R-band optical observations made with the MOSAIC-1 camera on the Mayall 4m Telescope of Kitt Peak National Observatory. Centered on the main FLS field, a region 9.4 square degrees in area was imaged. In addition, 2.3 square degrees covering the ELAIS-N1 field was also observed. Although originally the ELAIS-N1 field was planned to be part of the FLS program, the FLS observations of the ELAIS-N1 field have now been revised to a very deep 10'×10' pointing to evaluate the confusion limits of the MIPS instrument. The remainder of the ELAIS-N1 field will now be imaged as part of a larger survey in this region, a portion of the SWIRE *Spitzer* Legacy Survey (Lonsdale et al., 2003).

In section 2 we review the overall observing strategy and describe the MOSAIC-1 observations. In section 3 we discuss the techniques used in the data reduction including the astrometric and photometric calibration of the images. We describe in section 4 the data products made publicly available. We detail in section 5 the criteria used to detect, classify, and photometrically measure objects in the images. Section 5 also includes a description of the information available in our catalogs. In section 6 we examine the quality of the imaging data by comparing them with other available data sets. Finally, a brief summary is given in section 7.

2. Observations

The optical observations of the FLS region (centered at $17^h18^m00^s$ +59°30'00'', J2000) and

---

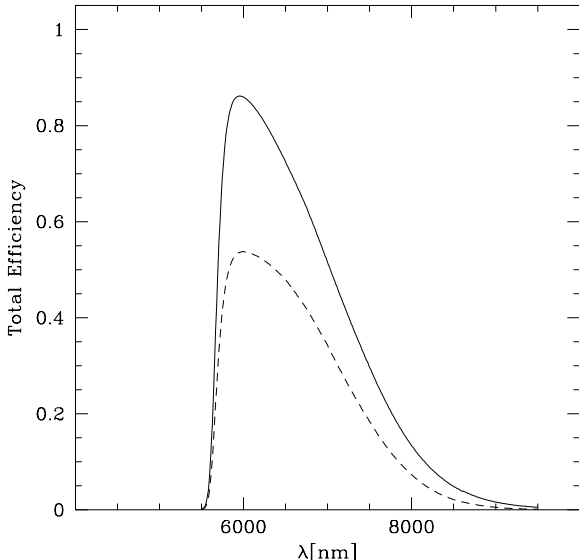[1]see the FLS website at ssc.spitzer.caltech.edu/fls

Fig. 1.— Transmission curve of the R-band filter (solid line) used for the observations. The dashed line indicates the combined response when considering also the CCD quantum efficiency, the throughput of the prime focus corrector, and the atmospheric absorption with a typical airmass of 1.2.

of the ELAIS-N1 region (centered at $16^h10^m01^s$ $+54^o30'36''$, J2000, see Oliver et al. 2000) were carried out using the MOSAIC-1 camera on the Mayall 4m Telescope at the Kitt Peak National Observatory. The MOSAIC-1 camera is comprised of eight thinned, back-illuminated SITe 2048 × 4098 CCDs with a projected pixel size of 0.258 arcsec (Muller et al. 1998). The 8 CCDs are physically separated by gaps with widths of approximately 14 and 15.5 arcsec along the right ascension and declination directions, respectively. The full field of view of the camera is therefore 36 × 36 square arcmin, with a filling factor of 97%. Observations were performed using the Harris Set Kron-Cousins R-band filter whose main features are summarized in Table 1. The transmission curve of the filter is shown in Figure 1 together with the resulting modifications that would be introduced by the corrector and camera optics, the CCD quantum efficiency, and atmospheric extinction.

For organizational purposes we chose to divide the proposed FLS survey region into 30 subfields each roughly the size of an individual MOSAIC-1 pointing. The coordinates of these subfields are listed in Table 2. During our observing run we were able to complete observations for 26 of these subfields. We similarly divided the ELAIS-N1 field into 12 subfields, but only completed observations for 5 of these fields. Each subfield was observed for a minimum of three 10 min exposures. In practice, some images were not suitable (poor seeing, flat fielding problem, or some other defect) and were not included in the final coadded or "stacked" images we are providing to the community. Table 2 lists in Col. 4 the number of exposures which were obtained and included in the coadded or "stacked" images. In order to provide some coverage in the regions of the sky that would fall in the inter-chip gaps, the positions of successive exposures of a given field were offset on order of an arcminute relative to each other. In general the first exposure was at the nominal (tabulated) position, the second shifted by 41.5' in α and −62.3' in δ, and the third with a shift of −41.5' and 62.3' in α and δ. In a few cases an additional position with $\Delta\alpha = 20.8'$ and $\Delta\beta = 31.1'$ has been observed. For a few fields, observations have been repeated due to the bad seeing or pointing errors.

The KPNO imaging observations were made on 2000 May 4-7,9 UT. A log of the observations is summarized in Table 3, which lists for each group of observations: the date of the observations (Col. 1); the subfield name (Col.2); the integration time and the number of exposures (Col. 3); and the seeing (delivered image quality expressed as FWHM in arcseconds of bright unsaturated stars) range of each exposure (Col. 4).

During a portion of the observing run, the pointing of the telescope was incorrectly initialized, resulting in approximately a 24' error in the pointing for some fields. These are noted in the observing log. Since the 24' offset did not map exactly on to our subfield grid, we chose to make stacked or combined images for several of the subfields. This was done for subfields # 11 and # 17 in the FLS region and subfields (# 6, # 9 and # 10) of ELAIS-N1. In Figures 2 and 3 we show the positions of each subfield on the sky with respect to the fields which have been covered with the IRAC and MIPS instruments on-board
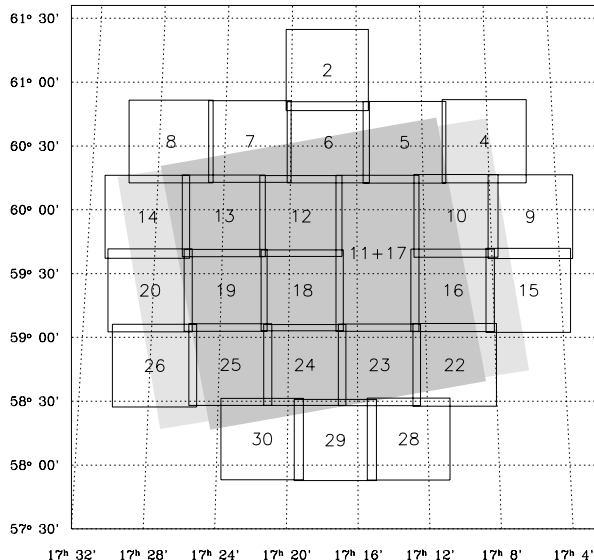
3

Fig. 2.— The KPNO fields in the FLS region cover most of the MIPS (grey) and IRAC (dark grey) Spitzer observations.

Spitzer. In Figure 3 we display the position of the subfields in the ELAIS-N1 region and the region observed with ISOCAM as part of the European Large Area ISO Survey (ELAIS, Oliver et al. 2000). The shaded square indicates the area which has been observed to test the confusion MIPS 24 micron confusion limits, as part of the FLS observations.

3. Data Reduction

3.1. Basic Reductions

The processing of the raw MOSAIC-1 exposures followed the steps outlined in version 7.01 of "The NOAO Deep Wide-Field Survey MOSAIC Data Reductions Guide"[2] and discussed by Jannuzi et al. (in preparation). The bulk of the software used to process the images and generate combined images for each subfield from the individual 10 minute exposures is described by Valdes (2002) and contained as part of the MSCRED software

package (v4.7), which is part of IRAF.[3]

The image quality of the final stacks is variable, as was the seeing during the run. Users of the images should be aware that the detailed shape of the point spread function in a given image stack could be variable across the field, not only because of residual distortions in the camera, but because a given position in the field might be the average of different input images, each with their own point spread function. No attempt was made to match the PSFs of the individual images before combining the images.

In a survey area this large there will be fields with very bright stars. This can cause some regions of the survey area to be impacted by scattered light from these stars. Some effort was made
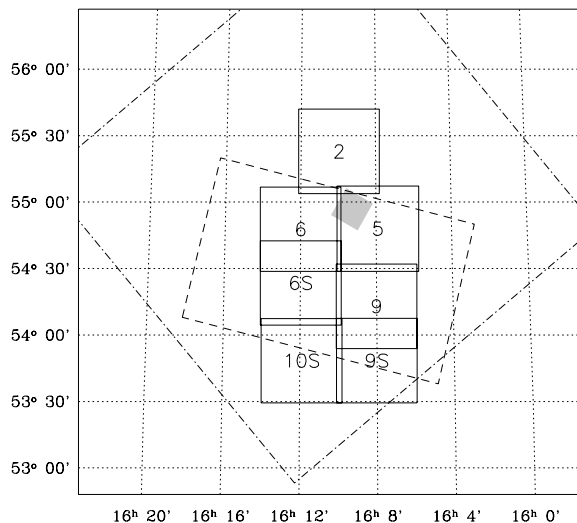
Fig. 3.— The KPNO fields in the ELAIS-N1 region. The dashed line corresponds to the region observed by ISOCAM at 14.3 μm (Oliver et al. 2000). The grey shaded square is the field observed with Spitzer to test the MIPS 24 micron confusion limit. The SWIRE planned field (Lonsdale et al. 2003) is marked with a dash-dotted line.

to minimize this impact during the observations (by shifting pointings) and reduction of the images (through masking of affected regions in some images to allow unaffected images to be the sole contribution to the stacked image), but users of the images should be aware that some scattered light will have made it into some of the stacks. An example of a subfield with significant scattered light is FLS_15.

Flat fielding of the images was accomplished through the application of calibration files generated first from observations of a flat-field screen inside the dome at the 4m and from a "super-sky" flat constructed by combining the majority of the FLS and ELAIS-N1 images (with objects masked and rejected). The result is generally excellent flat fielding of the sky (with some fields with slightly different sky color, due to moon light or twilight worse), but users should be aware that there are likely to be some color-dependent variations between and within the 8 CCDs, meaning that uncorrected errors in the photometry of a given object, attributable to the flat fielding correction not being derived from a source with color matched to the color of that object, on the order of 1 to 3 percent could still be present in the data even though the sky is generally quite "flat".

3.2. Astrometric Calibration

The astrometric calibration of the MOSAIC-1 images is accomplished in two steps. First, the high-order distortions in the field, which will in general be common to all our exposures (those anticipated to be the result of the optics and/or CCD placement and as a result stable over the course of an observing run or season) are calibrated using observations of an astrometric standard field. These distortions can be wavelength dependent, so the calibration is made for the specific filter being used. These images are analyzed to produce a default correction for each of the CCDs. Low-order corrections (translational offset, small rotation, and/or scale adjustments needed to compensate for pointing errors, instrument mounting variations between runs, and atmospheric effects) are corrected on an exposure by exposure basis using the many catalog objects in each exposure, the previously mentioned knowledge of the high-order distortions as a function of CCD position, and the software *msccmatch* in IRAF. The astrometric

calibration has been performed using the reduction protocol developed for the reduction of the NOAO Deep Wide-Field Survey (NDWFS) data which assumes as astrometric reference the USNO-A2.0 catalog (Monet et al. 1998). Adopting the GSC II catalog,[4] which became available after the development of the NDWFS reduction protocol, might improve the quality of the astrometric solutions and this might be done if a rereduction of the data set is done in the future. As we discuss further below, the anticipated improvement would be slight. For the images described in this paper our solutions for the mapping of the MOSAIC-1 pixels into a world coordinate frame had an RMS scatter of between 0.3 to 0.45 arcseconds, depending on the particular field.

After each image was provided with an improved astrometric calibration, it was tangent-plane projected with respect to the FLS and ELAIS-N1 field center positions listed above. Following projection, the individual exposures (typically three for a given region of the sky) could be combined into a final, stacked, image. These are the images currently being made available in the *Spitzer* and NOAO archives.

During the final stages of the data reduction, when the individual images were being combined to make the final image stacks, it was determined that there was an error in the high-order astrometric correction file for the Harris R-band filter affecting the adjacent edges of CCDs 7 and 8 in the MOSAIC-1 camera. The original solutions for the high order distortion terms were determined on a chip by chip basis with no requirement that the solution be continuous across the entire field. In general, while this requirement was not imposed, it was met by the solutions provided by NOAO. However, for the R-band the solution available at the time we were reducing the data was discon-

---

[4]The Guide Star Catalogue-II is a joint project of the Space Telescope Science Institute and the Osservatorio Astronomico di Torino. Space Telescope Science Institute is operated by the Association of Universities for Research in Astronomy, for the National Aeronautics and Space Administration under contract NAS5-26555. The participation of the Osservatorio Astronomico di Torino is supported by the Italian Council for Research in Astronomy. Additional support is provided by European Southern Observatory, Space Telescope European Coordinating Facility, the International GEMINI project and the European Space Agency Astrophysics Division.

tinuous at the CCD7 and CCD8 boundary. Since our image stacks are made from the combination of three or more images that are offset by 30 arcseconds to an arcminute from each other, this difference between the solutions for the two CCDs can result in a mis-mapping, into RA and DEC space, of a region of the sky imaged first on CCD7 and then on CCD8. The error is small, and introduces at most an additional $0.1''$ uncertainty to the positions of sources in the affected region (which is located in the SE Corner of each field, about 25% of the field up from the southern edge), but will result in a degradation of the PSF for objects affected in this region. The size of the affected region in each subfield is approximately $8.5'$ East-West and $2.5'$ North-South, or a bit less than 2% of the surveyed area.

3.3. Photometric calibration

Since not all the subfields were observed during nights with photometric conditions (see Table 3), we derived a coherent photometric system in two steps. First, we computed the relative photometric zero-points between the differ-

Fig. 4.— Dependence of zero-point on the airmass. Each squares is a standard star used in the calibration with 9 standard fields observed during the night of 2000 May 5.

ent stacked images of the subfields. Since each subfield overlaps its neighbor by approximately two arcminutes, we can estimate the extinction difference between them using a set of common sources. This can be expressed in terms of zero-point that, by definition, includes the effects of airmass and extinction. Because each frame has multiple overlaps, the number of frame-to-frame magnitude differences is over-determined with respect to the number of frames. Therefore, one can derive the relative zero-point for each frame simultaneously using a least squares estimator. We extracted the sources from each subfield using as a first guess for the zero-point that we computed for a central subfield (#18 and #5 for the FLS and ELAIS-N1 fields, respectively). For each overlap between contiguous fields, we selected the pairs of stars with magnitude $18 < R < 21$ and computed the median of the difference in magnitudes by using a 3σ clipping procedure. The magnitudes considered were the auto magnitudes (MAG_AUTO) from SExtractor, which are fairly robust with respect to seeing variations. To estimate the relative zero-points in the sense of the least squares, we minimized the sum:

$$\sum_{i>j} N_{ij}^2 (z_i - z_j - \Delta_{ij})^2, \qquad (1)$$

where z_i is the variation with respect to the initial guess of the zero-point of the subfield i, and Δ_{ij} is the median of the differences of magnitude for the set of the N_{ij} source pairs in the overlapping region between the subfields i and j. Solving the linear system obtained by imposing that the derivatives of (1) with respect each z_i are equal to zero, we corrected the initial guesses for the zero-points. The procedure was then iterated until the number of pairs N_{ij} became stable.

The second step was to make use of those fields observed under photometric conditions in order to converge on the best zero-point. Standards were measured several times over a broad range of airmasses on the first two nights of the observations, which had the best photometric conditions (see Table 3). Only the second night (May 5) was really photometric since all the measurements are coherent (see Figure 4). Magnitudes were calibrated to the Kron-Cousins system using Landolt standards taken from Landolt (1992). They have been obtained using an aperture of 6 arcsec in diameter,
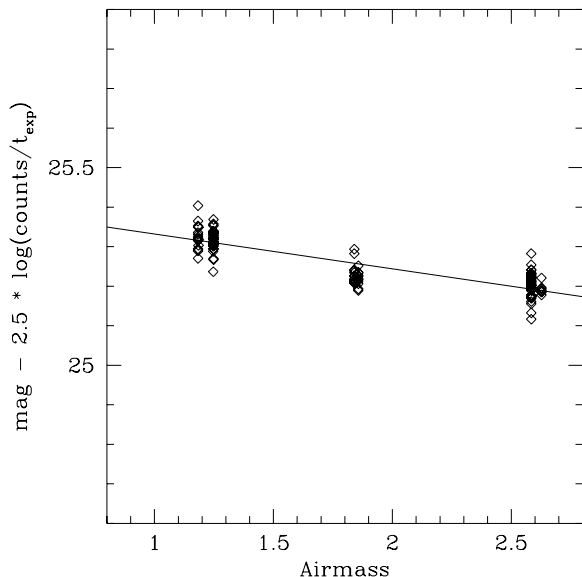
large enough to obtain accurate measurements according to the growth curves of all the measured stars. We have fitted the linear relationship:

$$m = m_0 - 2.5 \log(C/t_{exp}) + m_X * A, \quad (2)$$

with m magnitude of Landolt standard, A airmass during the observation, C counts during the exposure time t_{exp}, m_0 and m_X the zero and extinction terms, respectively. We used an iterative 3σ clipping in order to discard deviant measurements, finding the best fit for $m_0 = 25.42$ and $m_X = -0.09$. The standard deviation of the residuals for the best fit is 0.03.

4. Data Products

The analysis of the survey data produced a set of intermediate and final products, images and catalogs, which are publicly available at the Spitzer Science Center and NOAO Science Archives[5]. In particular, we provide the astronomical community with:

Coadded (Stacked) Images of the Subfields: sky-subtracted, fully processed coadded frames for each subfield. The subfields are mapped using a tangential projection. The size of each fits compressed image is 220 MB. For each image, a bad pixel mask and an exposure map is given (in the pixel-list IRAF format). The photometric zero-point of each subfield after the absolute photometric calibration of the frame appears in the header of the image. A full description of the header keywords is available at the http sites.

Low-resolution field image: sky-subtracted, fully processed coadded images of the whole field. The images have been created to give a general overview of the FLS and ELAIS-N1 fields and have been produced using a 1.3 arcsec pixel size (corresponding to five times the original size of the pixel). Users are discouraged from using them to extract sources and compute photometry. These images have a size of approximatively 380 Mb and 80 Mb.

Single subfield catalogs: object catalogs associated with each single subfield. A full description of the parameters available is described in the following Section. The catalogs are in ASCII format.

5. Catalogs

The main goal of this survey is to catalog galaxies and faint stars and make a first distinction between stars and galaxies on the basis of their intensity profiles. Several bright objects (mainly stars) are saturated and excluded from the catalog, but can be found in catalogs from shallower surveys (like the Sloan Digital Sky Survey in the case of the FLS region, see e.g. Stoughton et al. 2002 and Hogg et al. 2004). The source extraction was performed with the SExtractor package (Bertin & Arnouts 1996; ver. 2.3) which is well suited for surveys with low to moderate source density as is the case of our surveys.

5.1. Detection

Several parameters have to be fixed to achieve an efficient source extraction with SExtractor. The first problem is the evaluation of the background. SExtractor proceeds computing a *mini-background* on a scale large enough to contain several faint objects and filtering it with a box-car to avoid the contamination by isolated, extended objects. Finally, a full-resolution background map is obtained by interpolation and it is subtracted from the science image. In our case, many bright stars populate the FLS field since it has a moderate galactic latitude (34.9 degrees) while the problem is less important in the case of the ELAIS-N1 field (gal. latitude: 44.9 degrees). To evaluate a background which is not locally dominated by bright stars we adopted meshes of 128×128 pixels for the *mini-background* corresponding to 33.0 arcsec and used a 9×9 box-car for the median-filtering.

In order to improve the detection of faint sources, the image is filtered to enhance the spatial frequency typical of the sources with respect to those of the background noise. A Gaussian filter with an FWHM similar to the seeing of the image (in our case 4 pixels, since the overall seeing is 1.1) has been used. Although the choice of a convolution kernel with a constant FWHM may not always be optimal since the seeing is varying in the different images, the impact on detectability is fairly small (Irwin 1985). Moreover, it has the advantage of requiring no changes of the relative detection threshold.

Finally, the detection is made on the background-

subtracted and filtered image looking for groups of connected pixel above the detection threshold. Thresholding is in fact the most efficient way to detect low surface brightness objects. In our case, we fixed the minimum number of connected pixels to 15 and the detection threshold to 0.8 (in units of the standard deviation of the background noise), which corresponds to a typical limiting surface brightness $\mu_R \sim 26$ mag arcsec^{-2}. For the detection we made use also of the exposure map as a weight considered to set the noise level for each pixel. Some pixels have a null weight since they correspond to saturated objects, trails of bright objects and other artifacts. These pixels are also marked in the bad pixel mask and the false detections around these image artifacts are flagged and easily excluded from our final catalogs.

Only objects detected with a signal-to-noise greater than 3 (based on the total magnitude errors) are accepted in our final catalog.

Although not well suited to detect objects in crowded fields, SExtractor allows one also to deblend close objects using a multiple isophotal analysis technique. Two parameters affect the deblending: the number of thresholds used to split a set of connected pixels according to their luminosity peaks and the minimal contrast (light in a peak divided by the total light in the object) used to decide if deblending a sub-object from the rest of the object. In our analysis we used a high number of thresholds (64) and a very low minimal contrast (1.5 e^{-5}). Nevertheless, a few blended objects still remain in the catalogs. Visual inspection or other extraction algorithms more efficient in crowded fields (e.g, DAOPHOT) are needed to treat these particular cases.

5.2. Photometry

The photometry has been performed on the stacked images. Several measurements were made: aperture and isophotal magnitudes and an estimate of the total magnitudes. We measured the aperture magnitude within a diameter of 3 arcsec, roughly corresponding to three times the overall seeing. Total magnitudes (MAG_AUTO) are estimated using an elliptical aperture with an approach similar to that proposed by Kron (1980). Since these fields have been selected in sky regions with low Galactic extinction to observe extragalactic infrared sources, the corrections for Galactic

extinction (Schlegel et al. 1998) are small: 0.06 and 0.01 on average for the FLS and ELAIS-N1 fields, respectively.

The total magnitude of sources close to bright objects are usually inaccurate since the local background is affected by the halo of the bright objects and the Kron radius is not correctly computed. To improve the photometry for these sources we have subtracted bright saturated stars from the images and excluded from the catalogs the sources detected in square boxes around these stars where the subtraction is not correct. Moreover, we have considered bright extended galaxies and excluded from the catalogs all the sources inside the Kron ellipses of the galaxies. In fact, most of these sources are bright regions of the galaxies or their photometry is highly affected by the diffuse luminosity of the galaxies.

To subtract bright saturated stars from the images we have computed radial density profiles on concentric annuli around the stars. Then, after subtracting these profiles, we have removed the diffraction spikes by fitting their profiles along the radius at different angles with Chebyshev polynomials. As visible in Figures 5 and 6, the background is much more uniform and the spikes become shorter. This improves the photometry for the objects surrounding the stars and avoid the detection of faint false sources on the diffraction spikes.

The correction works well for most of the stars, although we exclude from the catalogs the immediate neighborhood. In the case of very bright stars (Fig 6), multiple reflections between the CCD and the optics make difficult the subraction of a median radial profile and a faint halo is still visible after the correction.

5.3. Star/galaxy separation

SExtractor uses a neural network to separate star-like from extended sources returning a stellarity index ($CLASS\_STAR$) with values between 1 (a perfect star-like object) and 0. The distribution of this index as a function of the magnitude in one of our fields (FLS18) is shown in Figure 7.

The standard neural network of SExtractor has been trained for seeing FWHM values between 0.02 and 5.5 arcsec and for images that have $1.5 <$ FWHM < 5 pixels. It is therefore perfectly suited
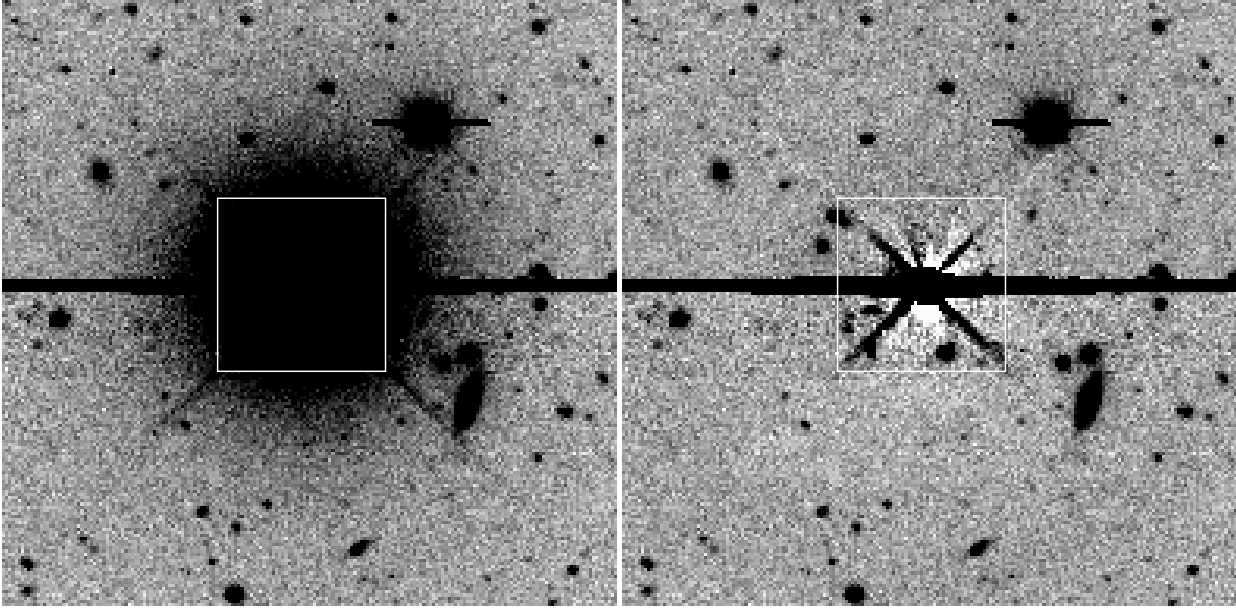
Fig. 5.— A 1.5'×1.5' field around a bright saturated star in the field FLS_6 before and after the star removal. The overplotted square delimits the region which is not considered in the final catalog.

Fig. 6.— A 7'×7' field around a bright saturated star in the field FLS_13 before and after the star removal. The overplotted square delimits the regi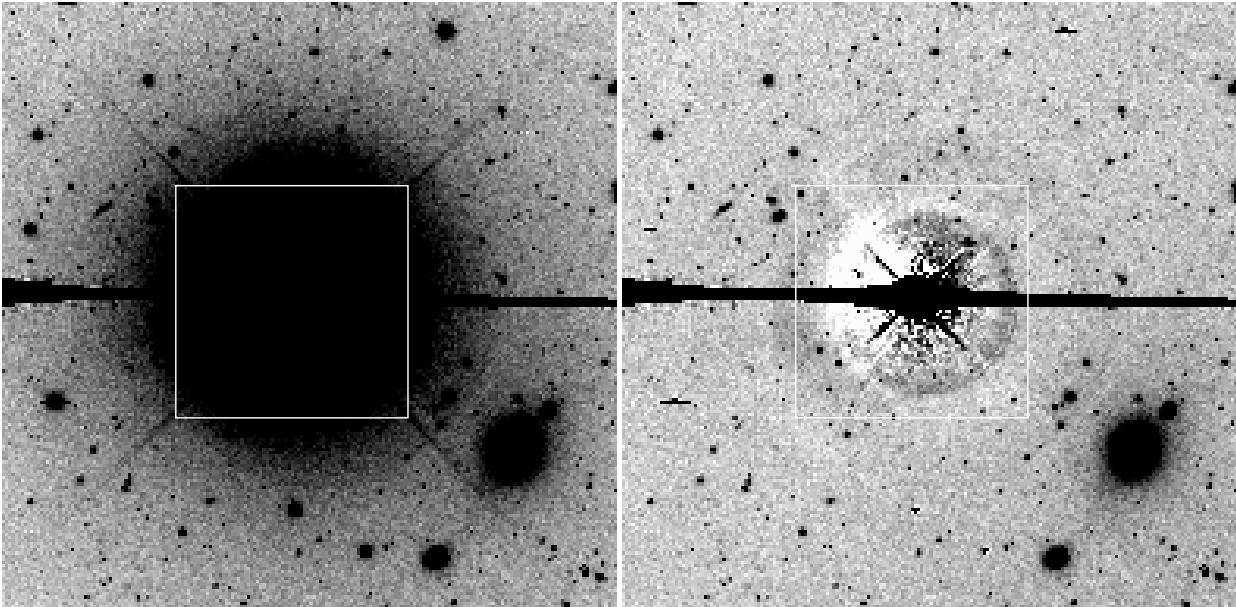on which is not considered in the final catalog. Multiple reflections of the star between the optics and the CCD are visible.
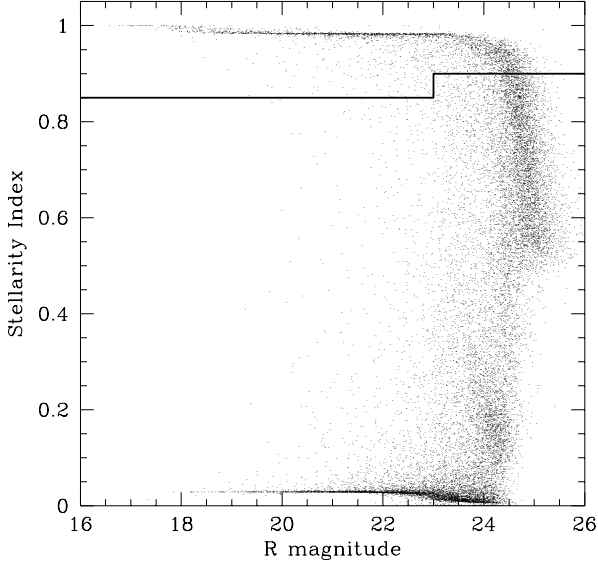
9

Fig. 7.— SExtractor stellarity index versus R magnitude for the objects detected in the field FLS18. The solid line indicates the threshold of the stellarity index as a function of the magnitude chosen to separate stars from galaxies in our survey.

for our images.

Although at bright magnitudes two sequences can be easily distinguished (see Figure 7), for fainter magnitudes it becomes more difficult to separate extended from point objects. In order to select stars in an efficient way, we followed the technique of Groenewegen et al. (2002) choosing a threshold which is a function of the magnitude. We consider that our objects are stars if:

$$CLASS\_STAR > 0.85 \qquad ... \text{ for } R < 23 \quad (3)$$
$$CLASS\_STAR > 0.90 \qquad ... \text{ elsewhere.} \quad (4)$$

A drawback of this technique is that at faint magnitudes QSOs are also classified as stars. However, using multi-band catalogs one can address the issue of separating stars and QSOs on the basis of their spectral energy distributions.

5.4. Source lists

As an illustration, the tabulation of the first 30 entries in the FLS_2 source catalog is presented in Table 4. All magnitudes are given in the Vega system. The Table lists:

- Column 1: the full IAU designation of the source;

- Columns 2-3: right ascension and declination (J2000);

- Columns 4-7: aperture (3 arcsec diameter) and total magnitudes and respective errors. The total magnitude corresponds to the MAG_AUTO magnitude measured by SExtractor. The magnitudes have been not corrected for Galactic extinction. The errors are those estimated by SExtractor and include only the shot-noise of the measured source and background counts. Only objects detected with signal to noise $S/N \geq 3$ (based on the total magnitude errors) and without saturated pixels are included.

- Column 8: an estimate of the S/N of the detection, from the errors estimated for the total magnitude;

- Column 9: the stellarity index computed by SExtractor;

- Column 10: the Galactic extinction taken from Schlegel et al. (1998).

All the catalogs in the archive are in ASCII format. Each catalog has been verified with several tests to check the reliability of the measured quantities with other sets of data. The results of some of these tests are described in the next section.

6. Survey performance

The characteristics of the data obtained by the present survey are summarized in Table 5 which lists: in Col. 1 the name of the subfield, in Cols. 2-3 the center of the subfield, in Col. 4 the seeing of the combined image, in Cols. 5-6 the 3σ and 5σ limiting R Cousin magnitudes, in Cols. 7-8 the number of galaxies and stars with $S/N \geq 3\sigma$ which are not saturated.

We measured the limiting R Cousin magnitude inside the aperture with the highest signal-to-noise ratio in case of a Gaussian PSF dominated by the
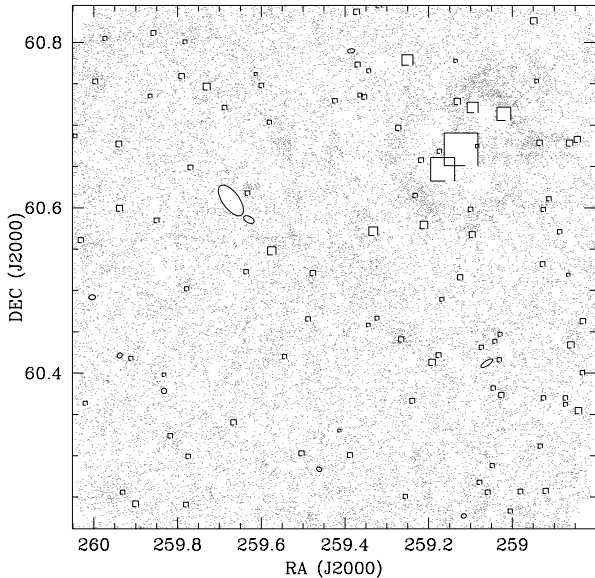
10

Fig. 8.— Projected distribution of galaxies extracted from the FLS_6 image. Square masks around the bright saturated stars and elliptical masks around bright extended galaxies in the field are shown.

sky. Considering a Gaussian profile, the S/N ratio inside an aperture R can be written as:

$$S/N = \frac{\int_0^R C e^{-2\ln 2r/W} dr}{\sqrt{\pi \frac{R^2}{\Delta^2} \sigma_S^2}}, \qquad (5)$$

with W, FWHM, C, central intensity of the source, Δ, pixel size, and σ_S, the sky noise. The R for which S/N is maximal corresponds to the R for which $\partial(S/N)/\partial R = 0$. This condition is realized at $R \approx 1.35W/2$, i.e. an aperture of $1.35 \times$ FHWM.

Since we are considering in our catalogs an aperture of 3 arcsec and our typical FHWM is 1.0 arcsec, these values are slightly deeper than what one can find in our catalogs.

The fraction of spurious objects was estimated by creating catalogs from the survey images multiplied by -1. Since ideally the noise is symmetric, we can use these images to produce a catalog of spurious sources by applying the same criteria of extraction which have been used with the real images. Analyzing the central square degree,

false-positive detections occur only at faint magnitudes (R>23.8). Considering all the 3σ objects, in the magnitude interval 23.5<R<24.5 there are 150 false-positive detection per sq. degree corresponding to 0.5% of the total number of sources. In the magnitude interval 24.5<R<25.5, there are 119 false-positive detections per sq. degree which correspond to 17% of the total of number of sources detected in this magnitude range.

6.1. Astrometry

To assess the accuracy of the astrometric calibration, we compared the positions of the stars inside the FLS field with those available from the Sloan survey (Stoughton et al. 2002, Data Release 1) and with radio sources from the VLA survey in the FLS field (Condon et al. 2003).

In the comparison with the Sloan sources, we considered only good objects (according to the flags) classified as stars in the Sloan catalog with R magnitude between 18 and 21. Table 6 reports the number of stars used in the comparison and the offsets between our and Sloan positions. Typ-
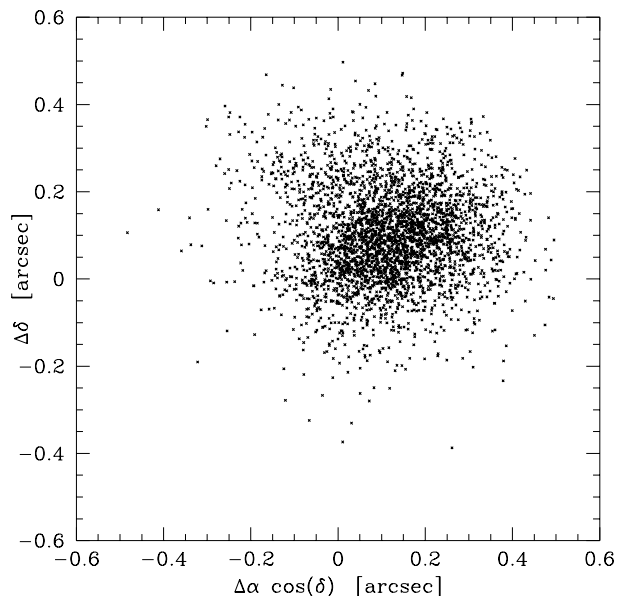

Fig. 9.— Comparison between the positions of stars in common with the Sloan survey for the field FLS-18. Offsets are computed as our minus Sloan positions.
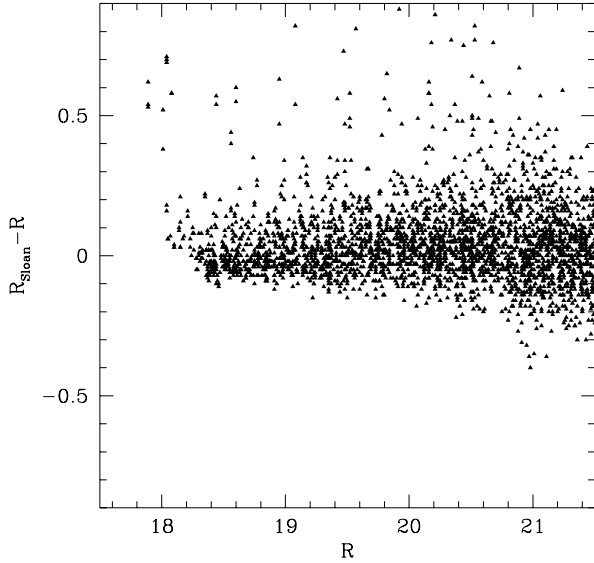
11

Fig. 10.— Comparison between the R magnitudes of stars in common with the Sloan Survey in the field FLS-18 as a function of the R magnitude (Vega system).

Fig. 11.— Offsets between our and Sloan magnitudes for stars with $18 < R < 21$ in the various FLS fields. The average difference is -0.007 ± 0.016.

ical offsets are 0.1 arcsec in right ascension and declination with an rms of 0.1 arcsec. The offsets between our catalog and the Sloan stars in the case of the field FLS-18 are shown in Figure 9. The comparison with the VLA sources has been made considering all the optical counterparts down to R=24 of non-extended radio sources. The offsets from the VLA positions are also of order 0.1 arcsec.

The systematic offset between ours and Sloan positions comes from the fact that our astrometry is based on the USNO-A2 catalog, while Sloan takes Tycho2 stars as reference. Comparing Sloan and USNO-A2 positions in the whole FLS field, we have an offset of $\Delta\alpha = 0.13 \pm 0.28$ and $\Delta\delta = 0.15 \pm 0.34$ arcsec which is in complete agreement with the offsets found in Table 6.

Finally, we compared our R-band catalog to the GSC II finding an offset of $\Delta\alpha = -0.05 \pm 0.18$ and $\Delta\delta = 0.22 \pm 0.15$ arcsec. While not large, this offset should be noted when making comparison to data sets that used the GSC II for reference.

Nevertheless, the remarkably small rms in both directions obtained comparing our and Sloan po-
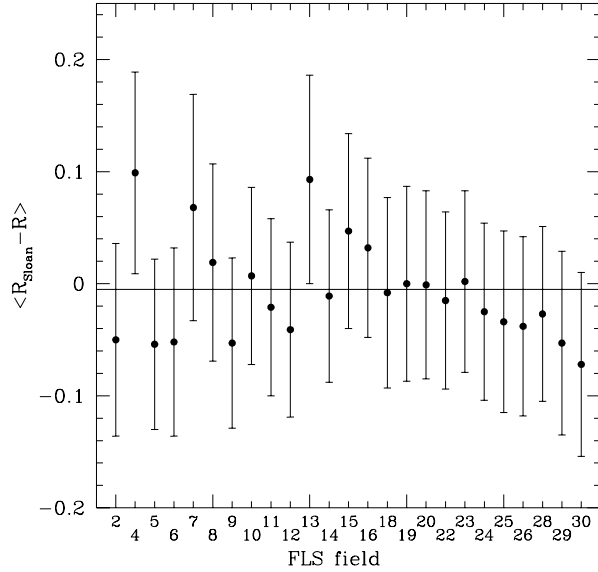
sitions suggests an intrinsic accuracy of $\lesssim 0.1$ arcsec for each catalog which is well within the requirements for slit/fiber positioning, an essential requirement for public surveys.

6.2. Photometry

The Sloan survey also allows us to compare the photometric calibration. Although the magnitude system used in this survey is different from ours, we can obtain a relationship between the R Cousin magnitude and the Sloan magnitudes using the 92 Landolt stars which have been observed by the Sloan group to calibrate their observations (Smith et al. 2002). Before making the comparison, we have converted the r' and i' magnitudes to the SDSS 2.5m natural system, using the equations:

$$r_{SDSS} = r' + 0.035\,(r' - i' - 0.21), \quad (6)$$
$$i_{SDSS} = i' + 0.041\,(r' - i' - 0.21), \quad (7)$$

as explained at the Sloan web site[6]. Then, we have obtained a relationship between R and the Sloan

---

[6]www.sdss.org/DR1/algorithms/jeg_photometric_eq_dr1.html

12

colors with a least square fit:

$$R = -0.16 + r_{SDSS} - 0.26 \, (r_{SDSS} - i_{SDSS}). \quad (8)$$

Using a biweight estimator, the difference between the real R and the value estimated with the relationship (8) is on average of 0.0001 (with an rms of 0.007). In spite of the large scatter, the relationship is useful from a statistical point of view since we are interested only in confirming our magnitude zero-point.

We have therefore compared the magnitudes of the stars in the FLS fields with the values deduced from the Sloan survey with the equation (8). Table 6 summarizes the median differences in magnitude between our measurements (*auto-magnitudes*) and the *model* complete magnitude as computed by Sloan for stars with magnitude $18 < R < 21$ in the different FLS fields. In Figure 10 we show the distribution of the magnitude offsets in the case of the central field FLS-18, while in Figure 11 we illustrate the offsets for the various fields. Our calibration agrees on average with the Sloan one, since the average difference between our and Sloan measurements is -0.007 ± 0.016. The biggest differences are found in the external subfields where the relative zero is not well constrained due to the low number of stars in common between adjacent subfields (see Figure 11).

6.3. Number counts

Counting galaxies and stars as a function of the magnitude allows one to evaluate the overall characteristics of a catalog as depth and homogeneity.

In Figures 12 and 14 we show star and galaxy counts in the FLS region and compare them with analogous counts using the Sloan Digital Sky Survey (Stoughton et al. 2002).

To compare the two distributions, we have transformed the SDSS magnitudes into the R Vega magnitudes using the relationship 8.

In the case of star counts (Fig. 12), the counts from our survey and the SDSS agree very well between R=18 and R=22. For magnitudes brighter than R=18, most of the stars detected in our survey are saturated and do not appear in our catalogs. Star counts drop very rapidly for magnitudes fainter than R=24 since the profile criterion used for the star/galaxy separation fails for faint objects. For comparison, we show in Figure 12 the
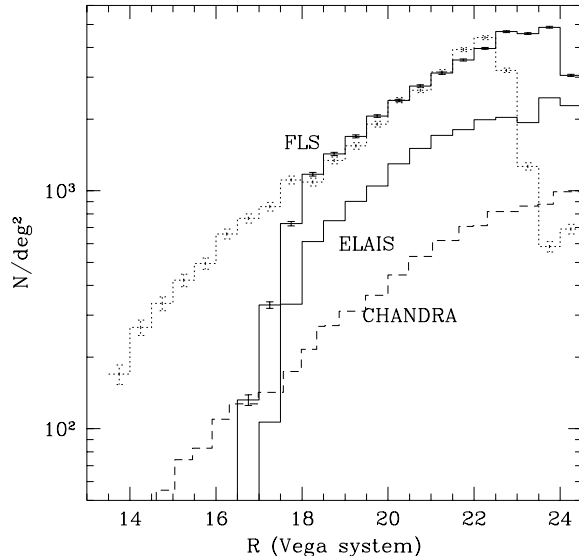

Fig. 12.— Star counts in the central square degree of the FLS region from our R images (solid line) and Sloan Digital Sky Survey catalogs (dotted line). For comparison, the dashed line refers to the counts in the Chandra South region (Groenewegen et al., 2002).

star counts in the ELAIS field and those in the Chandra field (Groenewegen et al., 2002). These fields, which lie at higher galactic latitudes are, as expected, less populated by stars.

To evaluate the variation in the number counts due to the varying observing conditions, we have computed the counts for each of the subfield in the FLS field. In Figure 13 we show these counts as well as the median counts with error bars corresponding to the standard deviation as measured from the observed scatter in the counts of the different subfields. One can easily see that a few subfields (#4, #7, #8, #15 and #26) are less deep than the other ones, as expected from the quantities measured in Table 5. Fortunately, these fields are external and have been only partially covered by Spitzer observations. The other 20 fields in the FLS are quite homogeneous.

Median counts are then reported in Figure 14 to compare them with the results from other surveys. The dotted line corresponds the counts from SDSS in the FLS field (Stoughton et al. 2002) com-
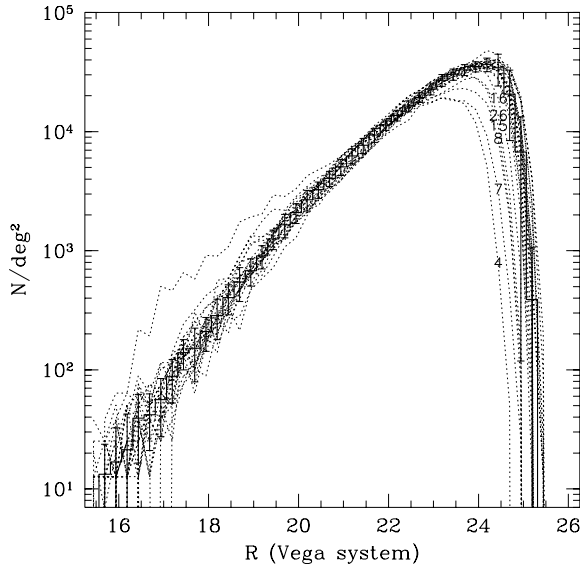
Fig. 13.— Galaxy counts in the various FLS subfields. The numbers refer to the FLS subfields with shallowest depths.

Fig. 14.— Galaxy counts in the FLS region from our R images (solid line) and Sloan Digital Sky Survey catalogs (dotted line). Results from counts in other sky regions are overplotted.

puted transforming the SDSS magnitudes into the R Vega magnitudes using the relationship in equation (8). The points from the general SDSS counts (Yasuda et al., 2001) have been approximatively transformed using the relationship by Fukugita et al. (1995) assuming that galaxies have $R - r'$ colors typical of spirals at redshift of $0.2 - 0.5$. At the faint end of the counts, results from several deep surveys are reported.

As an estimate of the completeness of our images we have compared our counts to the SDSS counts in the FLS field for R<21 and to median counts from the other deep surveys at magnitudes fainter than $R = 21$. In Figure 15 we show the completeness of the single subfields in the FLS field (thin lines) and those of the global field and the SDSS survey (continuous and dashed thick lines, respectively). Our survey is deeper than the SDSS data by almost three magnitudes. It is 50% complete around R=24.5. This estimate is conservative, since the number of spurious detection at R=24.5 is still relatively small (less than 0.5%).

Finally, for magnitudes brighter than R=18, the galaxy catalogs are slightly incomplete since a few extended objects are saturated.

7. Summary

A deep NOAO/KPNO survey in the R band has been carried out to observe a field of more than 9 square degrees centered at 17:18:00 +59:30:00 (J2000) aimed to find optical counterparts for the *First Look Survey* which surveys 7 different infrared wavelengths with the instruments IRAC and MIPS using the Spitzer Space Telescope. Another 2.3 square degrees have been surveyed in the ELAIS-N1 region which will be observed in the *Spitzer* SWIRE Legacy survey. This paper describes the observation strategy, the data reduction and the products which are publicly available to the astronomical community on the World Wide Web at the Spitzer Science Center and the NOAO Science Archives.

The overall quality of the data is good and homogeneous: the average seeing is 1.1 and typically varies between 0.9 and 1.2. The limiting magnitude of the images, measured inside an aperture of $1.35 \times$ FWHM for which the S/N ratio is maximal, is around R=25.5 at 5σ, deep enough to detect optical counterparts for a substantial fraction of the

Fig. 15.— Ratio between the number galaxies in our FLS survey and that of SDSS in the same region for $R < 21$ and that of median counts from several deep surveys at $R > 21$. Dotted thin lines show the completeness of single FLS subfields, while the dashed line shows the completeness of the SDSS survey in the FLS field.
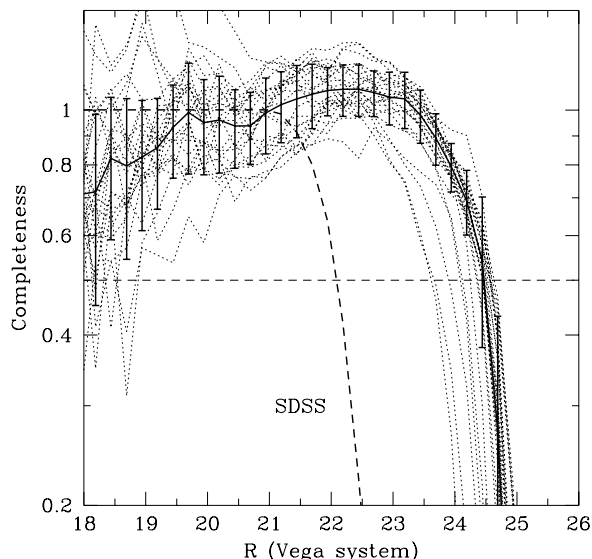
new *Spitzer* selected objects.

An average number of 35000 extragalactic sources are detected in each subfield (40' × 40', approximatively) with a 50% completeness limit of R=24.5 as deduced by comparing the counts with other deeper surveys.

Images and catalogs are available to the astronomical community along with the first release of the FLS infrared data to exploit in the best way the wealth of extragalactic data expected from the new infrared observatory *Spitzer*.

REFERENCES

Bertin, E., Arnouts, S., 1996, A&A, 117, 393

Brown, M. J. I., Dey, A., Jannuzi, B. T., Lauer, T. R., Tiede, G. P., & Mikles, V. J. 2003, ApJ, 597, 225

Condon, J. J., Cotton, W. D., Yin, Q. F. et al., 2003, AJ, 125, 2411

Dickinson, M. & Giavalisco, M., 2003, The Mass of Galaxies at Low and High Redshift, eds. R. Bender and A. Renzini, p. 324 (astro-ph/0204213)

Dole, H., Beichman, C. A., Egami, E., Engelbracht, C., Mould, J., Papovich, C.,Puget, J. L., Richards, P., Rieke, M. J., Rieke, G. H., 2001, BAAS, 199, 55.01

Fazio, G. G., Hora, Joseph L. W., Steve P., et al., 1998, Proc. SPIE, Vol. 3354, p. 1024.

Gallagher, D. B., Irace, W. R. & Werner, M. W., 2003, Proc. SPIE, Vol. 4850, p. 17

Groenewegen, M. A. T., Girardi, L., Hatziminaoglou, E., et al., 2002, A&A, 392, 741

Hogg, D.W., Blanton, M.R., Finkbeiner, D.P., Padmanabhan, N., & Schlegel, D.J., 2004, in preparation

Irwin, M. J., 1985, MNRAS, 214, 575

Jannuzi, B. T., & Dey, A. 1999, in ASP Conf. Ser. 191, Photometric Redshifts and High Redshift

Galaxies, ed. R. J. Weymann, L. J. Storrie-Lombardi, M. Sawicki, & R. J. Brunner (San Francisco: ASP), p. 111

Kessler, M. F., Steinz, J. A., Anderegg, M. E., et al., 1996, A&A, 315, 27

Kron, R. G., 1980, ApJS, 43, 305

Landolt, A. U., 1992, AJ, 104, 340

Lonsdale, C. J., Smith, H. E., Rowan-Robinson, M. et al, 2003, PASP, 115, 897

Metcalfe, N., Shanks, T., Fong, R., & Jones, L. R. 1991, MNRAS, 249, 498

Metcalfe, N., Shanks, T., Fong, R., & Roche, N. 1995, MNRAS, 273, 257

Monet, D. B. A., et al. 1998, "The USNO-A2.0 Catalogue", VizieR Online Data Catalogue

Muller, G. P., Reed, R., Armandroff, T., Boroson, T. A., & Jacoby, G. H., 1998, Proc. SPIE, 3355, 577

Oliver, S., Rowan-Robinson, M., Alexander, D. M. et al., 2000, MNRAS, 316, 749

Rieke, G. H., Young, E. T., Rivlis, G. & Gautier, T. N., 1996, BAAS, 28, 1274

Schlegel, D., Finkbeiner, D., & Davis, M., 1998, ApJ, 500, 525

Smail, I., Hogg, D. W., Yan, L., & Cohen, J. G., 1995, ApJ, 449, L105

Smith J.A., Tucker D.L., Kent S. et al., 2002, AJ, 123, 2121

Soifer, B.T., Neugebauer, G., Beichman, C.A., Houck, J.R., Rowan-Robinson, M. 1983, in Infrared technology IX; Proceedings of the Ninth Annual Meeting, San Diego, CA, August 23-25, 1983. Bellingham, WA, SPIE - The International Society for Optical Engineering, 297

Steidel, C. C., & Hamilton, D., 1993, AJ, 105, 2017

Stoughton, C., Lupton, R.H., Bernardi, M., et al. 2002, AJ, 123, 485

Tyson, J. A., 1988, AJ, 96, 1

Valdes, F. G., 2003, in "Automated Data Analysis in Astronomy", editors Ranjan Gupta, Harinder P. Singh, & Coryn A. L. Bailer-Jones, Narosa Publishing House, New Delhi, p. 309

Yasuda, N., Fukugita, M., Narayanan, V. K. et al., 2001, AJ, 122, 1104

TABLE 1

MAIN FEATURES OF THE FILTER USED IN THE MOSAIC-1 OBSERVATIONS.

Filter	KPNO ID	λ_{eff} Å	FWHM Å	Peak Throughput
R	R Harris k1004	6440	1510	86.2%

TABLE 2

NOMINAL COORDINATES OF THE OBSERVED SUBFIELDS.

ID	α (J2000)	δ (J2000)	Nr. of 10 minute obs.
FLS 2	17:17:48.12	+61:06:00.0	3
FLS 4	17:08:32.33	+60:32:00.0	3
FLS 5	17:13:13.17	+60:32:00.0	3
FLS 6	17:17:45.01	+60:32:00.0	3
FLS 7	17:22:25.85	+60:32:00.0	3
FLS 8	17:27:06.69	+60:32:00.0	3
FLS 9	17:05:44.94	+59:57:00.0	3
FLS 10	17:10:12.89	+59:57:00.0	5
FLS 11	17:14:48.65	+59:57:00.0	5
FLS 12	17:19:24.61	+59:57:00.0	4
FLS 13	17:23:59.47	+59:57:00.0	5
FLS 14	17:28:29.33	+59:57:00.0	3
FLS 15	17:05:56.30	+59:22:00.0	3
FLS 16	17:10:25.14	+59:22:00.0	3
FLS 17	17:14:54.99	+59:22:00.0	4
FLS 18	17:19:20.82	+59:22:00.0	4
FLS 19	17:23:53.67	+59:22:00.0	3
FLS 20	17:28:22.51	+59:22:00.0	3
FLS 22	17:10:18.66	+58:47:00.0	3
FLS 23	17:14:46.17	+58:47:00.0	3
FLS 24	17:19:12.00	+58:47:00.0	3
FLS 25	17:23:37.32	+58:47:00.0	3
FLS 26	17:28:02.83	+58:47:00.0	3
FLS 28	17:12:58.88	+58:12:30.0	3
FLS 29	17:17:19.44	+58:12:00.0	3
FLS 30	17:21:40.00	+58:12:30.0	3
ELAIS 2	16:10:01.00	+55:23:06.0	3
ELAIS 5	16:08:00.00	+54:48:06.0	5
ELAIS 6	16:12:06.76	+54:48:06.0	7
ELAIS 9	16:08:02.04	+54:13:06.2	9
ELAIS 10	16:12:06.76	+54:13:06.2	4

17

TABLE 3

LOG OF OBSERVATIONS.

Date	Subfield Number	Exposure Time (s)	Seeing Range (arcsec)	Photometric Conditions
2000 May 4	FLS04	3 × 600.	1.4-1.5	light cirri on sunset
	FLS05	3 × 600.	1.4-1.45	photometric
	FLS06	3 × 600.	1.5-1.6	
	FLS07	3 × 600.	1.2-1.5	
	FLS08	3 × 600.	1.2-1.3	
	FLS10	5 × 600.	0.98-1.15	
	FLS11	3 × 600.	0.97-1.15	
	FLS12	4 × 600.	0.79-1.3	
	FLS17	4 × 600.	0.8-0.95	
2000 May 5	ELAIS05	3 × 600.	1.07-1.25	photometric
	FLS15	3 × 600.	1.05-1.12	
	FLS16	3 × 600.	0.98-1.04	
	FLS20	3 × 600.	0.88-0.9	
	FLS19	3 × 600.	0.85-0.87	
	FLS18	4 × 600.	0.77-0.88	
	FLS24	3 × 600.	0.87-0.95	
	FLS23	3 × 600.	0.9-0.94	
	FLS22	3 × 600.	0.81-0.86	
	FLS25	3 × 600.	0.85-0.9	
	FLS13	1 × 600.	0.9	
2000 May 6	FLS13	4 × 600.	1.05-1.25	light cirri
	FLS11*	2 × 600.	0.95-1.1	non-photometric
	ELAIS06*	4 × 600.	0.88-0.95	
	ELAIS09*	4 × 600.	0.86-0.95	
	ELAIS10*	4 × 600.	0.87-1.0	
	FLS14*	4 × 600.	0.84-0.85	
2000 May 7	ELAIS02	3 × 600.	1.09-1.2	cirri
	FLS26	3 × 600.	1.0-1.2	non-photometric
	FLS28	3 × 600.	0.96-1.0	
	FLS29	3 × 600.	0.95-1.2	
	FLS30	3 × 600.	1.02-1.07	
	FLS09	3 × 600.	1.05-1.1	
	FLS02	3 × 600.	0.94-0.98	
	FLS05	3 × 600.	0.9-1.06	
	FLS06	3 × 600.	0.9-0.91	
	ELAIS05	2 × 600.	0.9-1.1	
	ELAIS06	3 × 600.	0.9-1.1	
	FLS14	3 × 600.	0.86-0.92	
2000 May 9	ELAIS09	5 × 600.	1.0-1.2	non-photometric

*A subfield observed 24' south of the originally intended position.

18

TABLE 4

FIRST 30 ENTRIES OF THE FLS_2 SOURCE LIST.

Identification (1)	α (J2000) (2)	δ (J2000) (3)	m_{aper} (4)	ϵ (5)	m_{tot} (6)	ϵ (7)	S/N (8)	Class (9)	Ext (10)
FLS_R_J171814.3+604643	17:18:14.303	+60:46:43.93	21.44	0.02	21.44	0.03	38.8	0.997	0.071
FLS_R_J171804.5+604644	17:18:04.511	+60:46:44.00	23.60	0.12	23.66	0.12	8.8	0.753	0.071
FLS_R_J171847.4+604644	17:18:47.496	+60:46:44.22	24.12	0.20	24.19	0.21	5.2	0.735	0.073
FLS_R_J171822.5+604644	17:18:22.536	+60:46:44.07	22.99	0.07	22.95	0.09	12.2	0.975	0.071
FLS_R_J171840.3+604644	17:18:40.368	+60:46:44.40	23.61	0.12	23.60	0.12	9.1	0.936	0.072
FLS_R_J171729.6+604645	17:17:29.639	+60:46:45.47	24.08	0.19	23.53	0.18	6.0	0.784	0.069
FLS_R_J171739.6+604645	17:17:39.672	+60:46:45.69	24.65	0.32	24.36	0.17	6.4	0.802	0.070
FLS_R_J171808.7+604643	17:18:08.784	+60:46:43.96	20.72	0.01	20.69	0.01	104.4	0.983	0.071
FLS_R_J171824.5+604644	17:18:24.575	+60:46:44.11	20.84	0.01	20.73	0.02	67.4	0.983	0.071
FLS_R_J171817.5+604644	17:18:17.567	+60:46:44.65	22.51	0.04	22.49	0.06	18.8	0.960	0.071
FLS_R_J171851.9+604644	17:18:51.984	+60:46:44.61	20.75	0.01	20.71	0.01	94.4	0.984	0.073
FLS_R_J171914.2+604645	17:19:14.232	+60:46:45.44	22.62	0.05	22.58	0.06	18.3	0.973	0.074
FLS_R_J171734.8+604646	17:17:34.872	+60:46:46.05	23.22	0.09	23.12	0.09	12.0	0.851	0.070
FLS_R_J171912.1+604647	17:19:12.191	+60:46:47.13	24.28	0.23	24.29	0.23	4.7	0.652	0.074
FLS_R_J171841.0+604646	17:18:41.087	+60:46:46.91	23.66	0.13	23.64	0.13	8.6	0.944	0.072
FLS_R_J171747.7+604648	17:17:47.712	+60:46:48.53	24.61	0.31	24.45	0.18	6.1	0.758	0.070
FLS_R_J171726.8+604646	17:17:26.807	+60:46:46.12	23.29	0.09	22.58	0.11	10.3	0.851	0.069
FLS_R_J171827.8+604646	17:18:27.887	+60:46:46.99	23.30	0.09	22.86	0.11	9.6	0.873	0.072
FLS_R_J171834.5+604648	17:18:34.560	+60:46:48.28	23.94	0.17	23.89	0.14	7.6	0.945	0.072
FLS_R_J171838.2+604644	17:18:38.279	+60:46:44.40	20.22	0.01	20.19	0.01	155.1	0.985	0.072
FLS_R_J171631.4+604647	17:16:31.487	+60:46:47.20	23.47	0.11	21.60	0.06	18.8	0.947	0.064
FLS_R_J171731.9+604646	17:17:31.967	+60:46:46.99	23.09	0.08	22.29	0.09	11.6	0.749	0.069
FLS_R_J171821.9+604645	17:18:21.911	+60:46:45.91	23.17	0.08	22.98	0.11	9.6	0.434	0.071
FLS_R_J171719.7+604649	17:17:19.704	+60:46:49.00	23.81	0.15	23.74	0.21	5.1	0.928	0.068
FLS_R_J171618.3+604647	17:16:18.312	+60:46:47.63	24.48	0.27	24.22	0.18	6.0	0.671	0.063
FLS_R_J171843.1+604648	17:18:43.128	+60:46:48.39	23.74	0.14	23.84	0.14	7.6	0.955	0.073
FLS_R_J171733.5+604649	17:17:33.503	+60:46:49.40	23.62	0.12	23.33	0.16	6.7	0.974	0.069
FLS_R_J171730.6+604649	17:17:30.671	+60:46:49.58	24.10	0.19	23.08	0.14	7.8	0.879	0.069
FLS_R_J171851.1+604645	17:18:51.143	+60:46:45.26	19.53	0.00	19.49	0.00	258.5	0.985	0.073
FLS_R_J171646.7+604647	17:16:46.751	+60:46:47.28	22.53	0.05	22.05	0.07	16.4	0.043	0.065

TABLE 5

PROPERTIES OF IMAGES AND EXTRACTED CATALOGS

ID	RA (J2000)	DEC (J2000)	Seeing (arcsec)	$m_{lim}(5\sigma)$ (mag)	$m_{lim}(3\sigma)$ (mag)	N_{gals}	N_{stars}
FLS 2	17:17:45.70	61:05:44.12	1.08	25.59	26.15	34766	6787
FLS 4	17:08:27.23	60:32:10.74	1.57	24.72	25.28	18016	2962
FLS 5	17:13:10.74	60:31:44.01	1.06	25.64	26.20	36372	5012
FLS 6	17:17:42.13	60:31:42.33	1.02	25.78	26.34	36988	5050
FLS 7	17:22:21.27	60:32:06.70	1.54	24.86	25.42	19959	1316
FLS 8	17:27:02.18	60:32:07.10	1.36	25.09	25.64	22392	3049
FLS 9	17:05:42.63	59:56:46.44	1.14	25.58	26.13	34985	5254
FLS 10	17:10:07.30	59:57:07.22	1.24	25.63	26.19	32253	3309
FLS 11-17	17:14:47.10	59:39:33.96	1.04	25.86	26.41	72709	6865
FLS 12	17:19:19.96	59:57:03.33	1.00	25.86	26.42	35905	4352
FLS 13	17:23:54.12	59:57:09.50	1.16	25.41	25.96	30797	5496
FLS 14	17:28:26.67	59:56:39.57	0.98	25.51	26.06	34672	5114
FLS 15	17:05:50.01	59:22:06.83	1.22	25.14	25.69	25218	4450
FLS 16	17:10:19.12	59:22:07.62	1.17	25.25	25.80	26996	4313
FLS 18	17:19:14.84	59:22:07.54	0.92	25.91	26.46	37922	4228
FLS 19	17:23:48.01	59:22:07.27	0.97	25.64	26.19	34771	4409
FLS 20	17:28:17.04	59:22:08.13	1.00	25.59	26.15	35297	4278
FLS 22	17:10:12.41	58:47:07.63	0.94	25.77	26.33	35201	4259
FLS 23	17:14:40.18	58:47:07.50	1.06	25.67	26.22	34624	4313
FLS 24	17:19:06.04	58:47:04.74	1.03	25.71	26.26	31151	4277
FLS 25	17:23:30.85	58:47:10.81	0.99	25.76	26.31	33847	4682
FLS 26	17:28:00.70	58:46:43.81	1.22	25.21	25.77	22636	5538
FLS 28	17:12:56.31	58:12:15.54	1.12	25.37	25.93	30609	5830
FLS 29	17:17:16.96	58:11:44.23	1.12	25.52	26.07	34524	6264
FLS 30	17:21:37.91	58:12:14.09	1.20	25.49	26.05	38493	10099
ELAIS 2	16:09:58.00	55:22:51.47	1.20	25.18	25.74	26960	3802
ELAIS 5	16:07:55.71	54:47:58.39	1.22	25.59	26.14	33876	3240
ELAIS 6	16:11:59.38	54:47:43.34	1.11	25.49	26.05	34736	3406
ELAIS 6S	16:11:58.89	54:23:29.02	0.98	25.82	26.38	41506	3160
ELAIS 9	16:07:59.66	54:12:59.29	1.11	25.77	26.32	38231	2926
ELAIS 9S	16:07:58.67	53:48:27.43	1.01	25.78	26.33	38167	3538
ELAIS 10S	16:11:56.45	53:48:23.99	1.02	25.72	26.28	36497	3496

TABLE 6

ASTROMETRY AND PHOTOMETRY: COMPARISON WITH SDSS AND VLA.

ID	Nr. of stars	$< R_{Sloan} - R >$ mag	$\alpha - \alpha_{Sloan}$ arcsec	$\delta - \delta_{Sloan}$ arcsec	Nr. of VLA sources	$\alpha - \alpha_{VLA}$ arcsec	$\delta - \delta_{VLA}$ arcsec
FLS 2	2004	-0.050±0.086	0.12±0.12	0.07±0.09	23	0.11±0.44	0.04±0.38
FLS 4	1523	0.100±0.090	0.19±0.12	-0.01±0.10			
FLS 5	1523	-0.054±0.076	0.12±0.12	0.07±0.09	84	0.09±0.34	0.24±0.35
FLS 6	1967	-0.052±0.084	0.17±0.13	0.15±0.10	117	0.17±0.37	0.28±0.36
FLS 7	1501	0.068±0.101	0.11±0.13	0.11±0.10	76	0.10±0.39	0.18±0.31
FLS 8	1571	0.019±0.088	0.14±0.13	0.18±0.09			
FLS 9	1319	-0.053±0.076	0.21±0.11	0.03±0.09			
FLS 10	1509	0.007±0.079	0.16±0.13	0.09±0.09	125	0.11±0.33	0.09±0.39
FLS 11-17	2810	-0.021±0.079	0.12±0.14	0.13±0.08	269	0.15±0.35	0.08±0.38
FLS 12	2132	-0.041±0.079	0.12±0.12	0.18±0.08	121	0.27±0.32	0.22±0.29
FLS 13	1412	0.093±0.093	0.09±0.14	0.15±0.10	128	0.08±0.37	0.12±0.37
FLS 14	1590	-0.011±0.078	0.08±0.13	0.10±0.09	29	0.07±0.35	0.13±0.47
FLS 15	1335	0.047±0.087	0.22±0.12	0.07±0.11			
FLS 16	1379	0.032±0.080	0.18±0.14	0.09±0.09	106	0.21±0.40	0.12±0.35
FLS 18	2294	-0.008±0.085	0.12±0.13	0.09±0.10	144	0.21±0.32	0.12±0.30
FLS 19	1614	-0.000±0.087	0.11±0.12	0.14±0.09	142	0.19±0.37	0.11±0.37
FLS 20	1608	-0.001±0.084	0.06±0.13	0.11±0.10	58	0.02±0.31	0.14±0.40
FLS 22	1461	-0.015±0.079	0.17±0.13	-0.11±0.10	61	0.30±0.35	-0.02±0.35
FLS 23	1510	0.002±0.081	0.10±0.15	0.03±0.09	121	0.09±0.35	0.07±0.37
FLS 24	2044	-0.025±0.079	0.03±0.13	0.07±0.12	143	0.05±0.38	0.07±0.37
FLS 25	2022	-0.034±0.082	0.04±0.12	0.05±0.09	117	0.13±0.38	0.08±0.36
FLS 26	1539	-0.038±0.080	0.05±0.13	0.00±0.09	34	0.04±0.40	0.17±0.40
FLS 28	1273	-0.027±0.078	-0.11±0.16	0.05±0.16			
FLS 29	1769	-0.053±0.082	-0.01±0.14	0.22±0.08	57	0.02±0.41	0.18±0.35
FLS 30	3198	-0.072±0.082	0.02±0.13	0.17±0.11	23	0.09±0.40	0.25±0.30
average		-0.007±0.016	0.10±0.03	0.09±0.02		0.12±0.08	0.13±0.08